



# Property-reactivity relations of N-doped PEM fuel cell cathode catalyst supports

Sebastian Ott<sup>a</sup>, Fengmin Du<sup>b</sup>, Mauricio Lopez Luna<sup>c</sup>, Tuan Anh Dao<sup>b</sup>, Sören Selve<sup>d</sup>, Beatriz Roldan Cuenya<sup>c</sup>, Alin Orfanidi<sup>b,\*</sup>, Peter Strasser<sup>a,\*</sup>

<sup>a</sup> Department of Chemistry, Chemical Engineering Division, Technical University of Berlin, Berlin, Germany

<sup>b</sup> BMW Group, 80788 Munich, Germany

<sup>c</sup> Department of Interface Science, Fritz Haber Institute of the Max Planck Society, 14195 Berlin, Germany

<sup>d</sup> Center for Electron Microscopy (ZELMI), Technical University of Berlin, Berlin, Germany

## ARTICLE INFO

### Keywords:

N-modification of carbon  
Oxygen reduction reaction  
Mesopore alteration  
Oxygen mass transport resistance

## ABSTRACT

This study clarifies the effect of the nature of solid N-precursor molecules on the N-modification, more specifically unravels how solid N-precursors – here cyanamide and melamine – affect the physicochemical and catalytic properties of the resulting carbon supports and final catalysts. Using such modified high surface area carbons, *in situ* measurements as humidity dependent performance, electrochemical surface area, proton resistivity and limiting current measurements were conducted to access the role and degree of ionomer coverage and transport resistances. Additional X-ray photoelectron spectroscopy (XPS) proves molecular interaction between acidic side chains and basic N-groups. Overall, we show the importance of the N-precursor and synthetic route determining which physicochemical parameter will be influenced in the resulting catalytic layer. Based on this, the pure presence of some N-moieties does not guarantee an improved ionomer distribution, but the modification process enables a tailoring effect of the carbon species itself affecting transport phenomena.

## 1. Introduction

To meet future economy and infrastructure zero emission goals, polymer electrolyte membrane fuel cells (PEMFCs) have been raising increased attention for automotive and stationary applications [1]. Nevertheless, further improvements are necessary to reduce production costs to realize further market penetration of fuel cell technology. One major issue is the sluggish oxygen reduction reaction (ORR) taking place on the cathode side, resulting in high demand of platinum group metals (PGMs) for the cathode reaction [2,3]. To achieve economically efficient automotive application, it has been proposed that the overall Pt loading per vehicle has to be reduced to below 5 g [4]. For this purpose, several approaches were made to realize Pt cathode loadings below 0.1 mg<sub>Pt</sub> cm<sup>-2</sup> without sacrificing fuel cell performance, whereas the state-of-the-art loading is around 0.3 mg<sub>Pt</sub> cm<sup>-2</sup> [1–3,5,6]. At the same time, automotive fuel cell stack operating strategy requires a highly mass active catalyst layer to achieve high PEMFC performance under low current densities [7]. Therefore, it is crucial to support the Pt nanoparticles on a high surface area carbon to reduce poisoning effects

from the ionomer compared to low surface area supported ones [3].

N-modification of cathode catalytic layers (CLs) have been purposed as a viable option to further improve high surface area carbons as support material [5,8,9]. The doping of carbon with N atoms either via solid precursors, NH<sub>3</sub>, plasma or other sources by completely manufacturing carbon e.g. for PGM-free catalyst is nothing new in literature [10–16]. Additionally, many Pt based N-modified catalysts have been reported which enhance certain electrochemical parameter. So, we first want to summarize some of the recently published work on N-modified carbon support for fuel cell application. Yang et al. demonstrated enhancement of ORR activity with Pt-alloy catalysts upon doping of the carbon black carbon support [17]. Better mass transport and lower ohmic losses were obtained by Prithi et al. while nitrogen-doping their mesoporous carbons [18]. Furthermore, Gribov et al. showed an improved utilization and increased ECSA (electrochemical surface area) for N-modified multi-wall carbon nanotubes using melamine as N-precursor [19]. N-modification via NH<sub>3</sub> was proven to promote more homogenous ionomer distribution, thus improved MEA performance and enhanced electrochemical stability [8,20,21]. Melamine as a N-source was

\* Corresponding authors.

E-mail addresses: [alin.orfanidi@bmw.de](mailto:alin.orfanidi@bmw.de) (A. Orfanidi), [pstrasser@tu-berlin.de](mailto:pstrasser@tu-berlin.de) (P. Strasser).

<https://doi.org/10.1016/j.apcatb.2022.121118>

Received 10 September 2021; Received in revised form 14 January 2022; Accepted 18 January 2022

Available online 20 January 2022

0926-3373/© 2022 Elsevier B.V. All rights reserved.

presented to result in structural changes of porosity and degree of order within the carbon matrix. For such modified graphene nanoplates, this leads to an overall better attachment of the Pt nanoparticles onto the carbon surface [22,23]. Despite these advances, fundamental insights into the nature of the carbon/ionomer interactions, in particular the carbon surface properties, as well as their effects at different relative humidity (RH), were still missing [24,25]. An extensive XPS study by Atanassov et al. investigated PGM-free catalyst layers with different ratios of N-functional groups, where it was found that the presence/amount of specific N-groups influences the ionomer side-chain/backbone alignment within the catalyst layer [26]. However, they did not investigate the effect of the synthetic route on the N/ionomer interaction nor the effect of the different N-groups on other electrochemical processes in the CL, such as mass transport, proton conduction or ECSA. Most published work about N-modified carbon supports for fuel cell application analyze the carbon and catalyst species mainly *ex-situ* and under RDE (rotating-disc electrode) configurations. Nevertheless, there is a commonly-known gap between RDE performance/configuration and real fuel cell operation [27]. Herein we try to bridge this knowledge gap and conduct some extensive fuel cell analysis correlating those findings with *ex-situ* determined changes of the carbon support introduced via N-modification. This study is attempting to shed some light onto this knowledge gap to better understand the complex interrelation between *ex-situ* material characterization and *in-situ* fuel cell performance. It is widely known that different *in-situ* measured catalyst layer properties, such as mass transport resistance and proton resistivity, strongly depend on the carbon support and layer characteristics.

In the present study, we investigate the chemical nature of the carbon/ionomer interactions of N-doped catalyst supports in PEMFCs under dry and wet conditions. To serve this purpose, we synthesized N-doped carbon supports using various solid precursors as nitrogen source. These precursors decompose at elevated temperatures and cause a chemical surface modification of the carbon materials [10,13,28–30]. As a result of the different modification temperatures and of the distinct chemical nature of the N-precursors, the physicochemical and catalytic properties of the N-doped carbons were altered. We probe and analyze the relations between these physicochemical properties of the modified carbon supports and their electrochemical and electrocatalytic processes inside the CL (e.g. proton conduction, mass transport, ECSA). In doing so, we identify the key properties of the carbon support that control their fuel cell power densities, and establish links to the associated synthetic routes. Taken together, our study provides synthetic guidelines as well as composition-structure-activity relationships of new N-modified platinumized fuel cell cathode carbon supports with improved performance.

## 2. Experimental methods

### 2.1. Oxidation of carbon

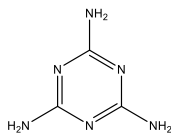
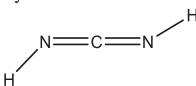
2 g of commercial carbon Ketjenblack EC-300J (AkzoNobel, here denoted as KB) was mixed with 100 mL 70% HNO<sub>3</sub> (VWR chemicals, Anala NORMAPUR) in a 250 mL flask. After the immersing of the suspension in a 70 °C pre-heated oil bath and stirring for 30 min under reflux, the suspension was filtered and rinsed with hot water until the pH of the filtrate became neutral. The final modified powder was received after dried in a vacuum oven at 80 °C for 17 h. The oxidized carbon is denoted as KBox.

### 2.2. N-functionalization of carbon

KB and KBox were subjected to various types of N-functionalization where the annealing temperature and N source were altered. Table 1 summarizes all synthesized types of N-functionalized carbon. To make a fair comparison among the samples, all the N functionalization was controlled by means of N excess ratio (see Table 1), so that the treated

**Table 1**

Summary of synthesized N-treated carbon samples detailing the corresponding treatment conditions (name of N precursor; temperature; KB/KBox) and the N excess defined as N-precursor to C-precursor ratio in mols of N and C.

	Melamine			Cyanamid		
						
Treatment Temperature	600 °C	600 °C	800 °C	600 °C	600 °C	800 °C
Oxidation in HNO <sub>3</sub>	No	Yes	No	No	Yes	No
Sample Name	KB-Mel-600	KBox-Mel-600	KB-Mel-800	KB-CA-600	KBox-CA-600	KB-CA-800
N mol/C mol	0.0016	0.0009	0.0108	0.0130	0.0081	0.0665

carbon exhibits a similar N weight percentage.

### 2.3. N-functionalization of carbon using solid N precursors

350 mg of the pristine carbon or pre-oxidized carbon has been merged with the corresponding amount of precursor (see Table 1). Here the initial weight of the C- and N-precursor is converted in its molar amount using the corresponding molar mass. From this, the molar C/N ratio is calculated considering the number of N atoms per N-precursor atom, i.g. one mole of melamine or cyanamide translates into six or two moles of nitrogen, respectively. The mixed precursors were diluted in 4 mL water and sonicated for 15 min to ensure a homogenous distribution and dissolution of the precursor. The suspension was subsequently frozen in liquid nitrogen and the water content evaporated in a freeze dryer overnight. The resulting powder was placed in a tube furnace (CARBOLITE GERO GmbH & Co KG, Germany) for N modification. A similar procedure of flushing, heating, holding, and cooling was applied as described in Ott et al [8], with the only difference of replacing all NH<sub>3</sub> flows by a N<sub>2</sub> flow (5 L/h). Two different set temperatures of 600 °C and 800 °C were applied.

### 2.4. Catalyst synthesis-Pt deposition

Pt was deposited on all carbon supports (including the pristine KB as reference) using a polyol-method described in detail in a previous work [8]. In short, 300 mg of the N-functionalized carbon was mixed with 200 mL ethylene glycol (99.8%, Sigma Aldrich) and 100 mL deionized water in a 500 mL round bottom flask [5], where H<sub>2</sub>PtCl<sub>6</sub> solution (0.25 mol/L, obtained from solid H<sub>2</sub>PtCl<sub>6</sub>·6H<sub>2</sub>O, Alfa Aesar) was added to the dispersion and stirred for overnight at 25 °C. The dispersion was immersed in a 120 °C pre-heated oil bath and stirred for 2 h under reflux. The obtained catalysts were filtered and rinsed with hot water (3 L per 200 mg sample) and were dried in a vacuum oven at 70 °C overnight. The nominal Pt loading was set between 16 and 20 wt% Pt depending on the type of carbon. The final Pt loading of the catalysts was obtained via ICP-OES and is shown in Table 2.

### 2.5. Induced coupled plasma optical emission spectrometry

To determine the exact Pt loading of the catalyst inductively coupled plasma (ICP) analysis was conducted using a VARIAN 715-ES system. For doing so, 7–11 mg catalyst powder was mixed with 2 mL H<sub>2</sub>SO<sub>4</sub> (95–98%, VWR chemicals, Anala NORMAPUR), 2 mL HNO<sub>3</sub> (69%, VWR chemicals, Anala NORMAPUR) and 6 mL HCl (37%, VWR chemicals, Anala NORMAPUR) in a microwave tube. The heating procedure in a microwave (Microwave GO, ANTON PAAR) was applied to conduct the chemical digestion. Herby, the suspension was constantly heated up to

**Table 2**

Cathode specifications of 5 cm<sup>2</sup> MEAs: Pt catalyst loading and crystallite size on different carbon supports evaluated by ICP and XRD respectively, average Pt particle size determined by TEM as well as the cathode Pt loading after decal transfer. The error bars represent the mean absolute deviation from two independent measurements.

Catalyst type	Pt <sub>ICP</sub> catalyst loading [wt %]	Pt <sub>XRD</sub> particle size [nm]	Pt <sub>TEM</sub> particle size [nm]	Pt <sub>MEA</sub> loading [mgPt/cm <sup>2</sup> <sub>MEA</sub> ]
Pt/KB	16.7	2.2	2.3 ± 0.4	0.108 ± 0.000
Pt/KB-Mel-600	18.4	1.9	2.3 ± 0.5	0.135 ± 0.005
Pt/KB-Mel-600	18.1	2.0	2.3 ± 0.5	0.135 ± 0.015
Pt/KB-Mel-800	20.1	2.1	3.1 ± 0.6	0.135 ± 0.015
Pt/KB-CA-600	18.4	2.2	2.4 ± 0.5	0.130 ± 0.010
Pt/KB-CA-600	18.4	2.0	3.3 ± 0.7	0.125 ± 0.015
Pt/KB-CA-800	17.9	2.2	2.5 ± 0.4	0.125 ± 0.015

120 °C within 10 min and kept there for another 10 min. For exact Pt determination, a calibration curve was constructed from standard solutions of 1, 5 and 10 mg/L (H<sub>2</sub>PtCl<sub>6</sub> in 2 mol/L HCl, 1000 mg/L Pt, MERCK KGAA) and specifically chosen wavelengths as 212.863 nm, 214.424 nm, 217.468 nm, 224.552 nm.

## 2.6. X-Ray diffraction

The Pt Particle size was determined by XRD from a BRUKER D8 ADVANCE diffractometer with a single beam and a Cu-K<sub>α1</sub> (γ = 1.54051 Å). The average Pt particle size was found to be 2.1 ± 0.1 nm. XRD spectra are shown in SI (Fig. S8).

## 2.7. Elemental analysis

To determine the elemental composition of C, H, N and S (Table 3), a Thermo Flash 1112 Organic Elemental Analyzer (Thermo Finnigan) has been used. Hereby, the samples were combusted by dynamic flash at 1020 °C where V<sub>2</sub>O<sub>5</sub> was added as oxidizer. The decomposition takes place in a manually stacked reactor of WO<sub>3</sub>/Cu/Al<sub>2</sub>O<sub>3</sub> layers, where the resulting gases were identified and quantified via Gas chromatography (GC).

## 2.8. Microstructure analysis

A detailed micro and meso pore analysis of various carbon supports was conducted determining N<sub>2</sub> physisorption isotherms at 77 K using Autosorb-1 (Quantachrome Instruments). For this purpose, the samples were placed in a 4 mm diameter glass tube stacked with glass wool and a glass rod to reduce the dead volume. To minimize measurement errors, the absolute weight of the sample mass was estimated to exceed an absolute surface area of 10 m<sup>2</sup> for each test. The samples were degassed under vacuum at 90 °C for around 24 h to remove any gas and water adsorbates. To avoid any functional group decomposition, the

**Table 3**

Elemental bulk composition (CHN) of the different types of carbons. The oxygen content was estimated as the difference to 100% assuming only C, N, H and O atoms in the modified carbon support.

Sample	Elemental analysis (wt%)			
	C	N	H	O
KB	98.57	0	0	1.43
KBox	90.00	0.11	0.21	9.68
KB-Mel-600	96.82	0.93	0	2.25
KBox-Mel-600	95.39	1.13	0	3.88
KB-Mel-800	97.65	0.73	0	1.62
KB-CA-600	96.19	0.94	0	2.87
KBox-CA-600	95.74	1.29	0	2.97
KB-CA-800	96.69	0.78	0	2.53

outgassing temperature was set as low as 90 °C. The adsorption and desorption isotherms were recorded in a range of  $10^{-5} \leq p/p_0 \leq 0.995$  with  $p$  referring to the actual gas pressure and  $p_0$  the saturation pressure. A Quenched solid density functional theory (QSDFT) kernel with a slit/cylindrical pores model was applied for the adsorption branch to derive the pore size distribution (micropores (< 2 nm) and mesopores (> 2 nm)). This kernel considers a certain surface heterogeneity and roughness, thus preventing artificial gaps in the evaluation [31–33]. To investigate pore blockage of the carbon pores by ionomer, CL comprised of the carbon+ionomer with an I/C ratio of 0.65 were analyzed and evaluated as described for the pure carbon supports above.

## 2.9. Water physisorption

A Quantachrome Hydrosorb 1000 instrument was employed to determine the water uptake of various carbon supports at 298 K. The samples were left for 72 h at 120 °C at  $10^{-3}$  bar to remove all traces of water. Each sample was He-calibrated before testing to define the exact weight. The analysis gas water was regulated to 100 °C from a manifold. Each testing-point was equilibrated within a pressure tolerance of 0.05 and equilibration time/equilibration timeout of 300/4000 s, thus resulting in an overall analytic time of 65 h.

## 2.10. Thermogravimetric analysis (TGA)

Thermogravimetric analysis was employed to evaluate the thermal stability of the surface groups present on pristine, oxidized and N-modified carbon supports. The measurements were conducted on a TGA-DSC PERKINELMER STA-8000 under Ar flow, where a heating rates of 5 K/min was used to reach 1100 °C.

## 2.11. X-ray photoelectron spectroscopy

For the evaluation of the elemental and chemical state of the surface groups present on the different carbons, the samples were treated in ultrahigh vacuum (UHV) at room temperature using a monochromatized Al K<sub>α</sub> X-ray source (1486.6 eV) excitation and a hemispherical analyzer (Phoibos 150, SPECS). Spectra alignment was according to C 1s graphitic peak (284.5 eV). A flood gun (SPECS FG 15/40) was used for samples exhibiting charging to compensate for any surface charge. Theoretical cross-sections from Yeh et al. were used to calculate the elemental surface composition [34]. 8 components with individual binding energies (indicated in parenthesis) were used for N 1s spectra fitting: pyridinic N (398.4 eV), hydrogenated/protonated pyridinic N (399.7 eV), pyrrolic N (399.9 eV), quaternary N (401.1 eV), protonated pyridinic N (401.7 eV), graphitic N (402.4 eV), hydrogenated graphitic N (403.8 eV) and N-oxide species (404.1 eV) [35–39]. Data processing was performed using the CasaXPS software. All components were fitted using Voigt type line shapes, Shirley background and FWHM of 1.5–1.6 eV.

The ionomer and carbon support interaction were investigated by analyzing carbon/ionomer electrodes. For this purpose, electrodes consisting of various types of carbon supports and ionomer with an I/C ratio of 0.25 were manufactured and subject to XPS analysis. The manufacturing procedure for the carbon/ionomer XPS samples is similar as for the MEA ones and described in the following section “MEA preparation”.

## 2.12. Transmission electron microscope (TEM)

TEM measurements were conducted using a Tecnai G2 20s-Twin microscope, equipped with a LaB<sub>6</sub>-cathode and a GATAN MS794 P CCD-detector at ZELMI Centrum, Technical University of Berlin. The samples were ultrasonicated in *i*-ProH and drop-dried on TEM copper grids. TEM imaging was used to evaluate the Pt particle size distribution and calculate the theoretical ECSA by analyzing approximately 100

particles from several high magnification TEM micrographs for each sample: i)  $d$  corresponds to the number averaged particle diameter and its standard deviation (SD); ii)  $d_s$  is the surface-averaged diameter, defined as  $d_s = \Sigma d_i^3 / \Sigma d_i^2$  and its standard deviation which is derived in Eqs. (1) and (2); iii) ECSA<sub>TEM</sub> is the TEM derived electrochemically active surface area, defined as ECSA<sub>TEM</sub> =  $6/(d_s \cdot \rho)$  with  $\rho$  being the density of platinum.

$$SD_s = \left( \frac{\partial D_s}{\partial d} \right) \cdot SD \quad (1)$$

$$SD_s = \left[ 3 - \frac{(2 \Sigma d_i^3)(d)}{(\Sigma d_i^2)^2} \right] \cdot SD \quad (2)$$

### 2.13. Membrane electrode assembly (MEA) preparation

The decal transfer method was applied for the manufacturing of all MEAs [40]. The catalyst ink was prepared using a low-EW ionomer dispersed in 40% H<sub>2</sub>O/60% 1-propanol (3 M™ Dyneon™ PFSA (725 EW  $\equiv$  g<sub>polymer</sub>/mol<sub>H+</sub>)) that was mixed with the catalyst powder. The catalyst ink has a specific water/1-propanol ratio of 16–25 wt% H<sub>2</sub>O in 1-propanol. After optimizing the ink recipe and viscosity to achieve high decal quality, all materials were merged in a 15 mL HDPE capped bottle containing 26 g of 5 mm ZrO<sub>2</sub> beads in the following sequence: catalyst, water, 1-propanol, and finally the ionomer dispersion. The bottles were placed onto a roller-mill (60 rpm) for 18 h at room temperature for homogenous mixing. Finally, the inks were coated onto virgin PTFE using a Mayer rod coater (ERICHSEN UNICOATER MODEL 490) with a coating speed of 10 mm/s. A summary of the cathode specifications can be found in Table 2. All tested cathodes had an ionomer to carbon (I/C) mass ratio of 0.65 and an average catalyst loading of  $0.124 \pm 0.016$  mg<sub>Pt</sub>/cm<sup>2</sup> (specifications of each catalyst type per MEA type are given in Table 2).

For the anodes, commercially available 30 wt% Pt/graphitized-Ketjenblack (TEC10EA30E, TANAKA Kikinzoku Kogyo K. K.) was used for electrode manufacturing. The I/C was set to 0.65 and Pt loading of 0.17 mg<sub>Pt</sub>/cm<sup>2</sup>. All electrode loadings (anode/cathode) were determined by weighing the decals before and after the catalyst layer transfer. The decal transferred membrane electrode assembly (MEA) was assembled by hot pressing (LAUFFER PRESSEN, type: UVL 25.0) a 10  $\mu$ m membrane (GORE, type: MX20.10) between the anode and cathode decals at 155 °C for 3 min with an applied force of 0.24 kN/cm<sup>2</sup>. The MEA was sandwiched between two subgaskets (CMC Klebetechnik, type: PEM-Schutzfolie 61325). The size of the subgasket window defines the MEA active area of 5 cm<sup>2</sup>. For the final MEA lamination in the subgasket, a 10 min hot press procedure at a set temperature of 135 °C was first conducted with an applied force of 0.135 kN/cm<sup>2</sup> over the entire area. Thereafter, the hot press temperature was ramped down to 75 °C within 10 min without releasing the pressure. A final sandwiched MEA placed between two hard sealings is shown in Fig. S1.

## 3. Electrochemical testing and diagnostics

### 3.1. Fuel cell assembly and testing

All the electrochemical testing for 5 cm<sup>2</sup> MEAs were conducted in a modified single-cell hardware from Tandem Technologies containing a 50 cm<sup>2</sup> active area graphite composite flow field (14 channel serpentine flow field [41] purchased from Nisshinbo). The flow field and adjustment of the MEA is shown in Figs. S1 and S2. A hardstop sealing approach is used to define the compression of the MEA, which is determined by the thickness of the sealing layers. The incompressible fiberglass-reinforced PTFE-gaskets (Fiberflon) was adjusted to obtain a  $20 \pm 1\%$  compression of the GDL (29 BCE with a nominal thickness of 235–240  $\mu$ m; SGL Carbon) by applying 9 bar clamping pressure. All fuel

cell measurements were conducted on an automated a HORIBA FuelCon GmbH (Germany) single cell test station (typ 200A FUELCON) equipped with a potentiostat (ZAHNER-Elektrik GmbH & CoKG) and additionally coupled with a booster. Pure hydrogen (99.999% purity) and compressed air were used as anode and cathode reactant, respectively. For each type of MEA, two independent fuel cell measurements were performed and the average value with corresponding error bars as the standard deviation is depicted in all figures.

All MEAs were conditioned using a protocol from Department of Energy (DOE), where the voltage was cycled 8 times between OCV (5 min), 0.85 V (10 min) and 0.6 V (45 min) at 80 °C cell temperature, 100% relative humidity (RH) at both anode and cathode and 170 kPa<sub>abs</sub> under differential flows (H<sub>2</sub>/air = 1.0/2.0 NL/min). The MEA performance was evaluated via two types of polarization curves (based on EU harmonized protocol [4,42]) under differential flows (H<sub>2</sub>/air = 1.0/2.0 NL/min): herein defined as “dry operating conditions” (90 °C cell temperature, 30% RH and 170 kPa<sub>abs</sub>) and “wet operating conditions” (60 °C cell temperature, 90% RH and 170 kPa<sub>abs</sub>). At specific current densities (0.1, 0.5, 1.0 and 2.0 A/cm<sup>2</sup>) during the polarization curve acquisition, galvanostatic EIS spectra (using the Zahner potentiostat) were recorded with starting frequency of 20 kHz up to 10 MHz to determine and monitor high frequency resistance (HFR). Since the monopolar plates/flow field are made of graphite composite material with a relatively high resistance of 30.5 m $\Omega$  cm<sup>2</sup>, relatively high HFR values are to be expected. In order to determine the real MEA resistance, the resistance of the monopolar plates is subtracted from the measured HFR values. Analogously, the polarization curves are corrected for the monopolar plate resistances.

The electrochemical active surface area (ECSA) of the cathode was evaluated via CO stripping under ambient pressure, with cell temperature of 80 °C, where the RH was set to 30% and 100% for each measurement (same value for anode and cathode). The anodic flow was kept constant at 500 nccm H<sub>2</sub>, while at the cathode CO was being adsorbed (0.2 NL/min of 0.1% CO in N<sub>2</sub>) for 30 min at holding the potential of 0.1 V. Thereafter, the cell was purged for 30 min using a N<sub>2</sub> flow rate of 0.5 NL/min to remove all CO residues in the gas phase while keeping the cell voltage at 0.1 V. To remove the absorbed CO, cyclic voltammetry (CV) was performed between 0.053 and 1.0 V, with a scan rate of 50 mV/s. To verify the complete removal of CO in the gas stream and the electrode surface, two additional sweeps were recorded. For more details refer to Du et al. [43].

Protonic resistivity of the cathode CL was obtained by applying AC impedance spectroscopy at 0.5 V with peak-to-peak perturbation of 20 mV under H<sub>2</sub>(anode)/N<sub>2</sub>(cathode) flows (1.0/2.0 NL/min). The cell temperature was constant at 80 °C. The RH was set to 30% and 100% (same for both anode and cathode). The EIS protocol used in this study and the determination of the specific proton resistivity ( $\rho$ , in  $\Omega$  cm) via fitting of the transmission line model was the same as described in detail in Du et al. [43]. Limiting current measurements were performed to determine the total O<sub>2</sub> mass transport resistances. The measurements were conducted at 30% RH and 100% RH at 80 °C cell temperature. Flows were kept constant at 1.0 NL/min H<sub>2</sub> and 2.045 NL/min diluted air (2.4% O<sub>2</sub>, 0.235 NL/min air + 1.81 NL/min N<sub>2</sub>). Similar testing procedure and protocol were used as described in Jomori et al. [44] and Du et al. [43]. The measurements were conducted at 170, 230 and 300 kPa<sub>abs</sub> with 5 min holding time at 0.3 V and 2 min at 0.2 V.

## 4. Results and discussion

### 4.1. Carbon and catalyst characterization

To investigate the influence of the N-functionalization of the catalyst support on its MEA performance, a set of distinct N-functionalized carbons using cyanamide and melamine was synthesized. The synthetic routes are given in detail in the experimental section above.



#### 4.2. Elemental analysis

As shown in Table 3, CHNO elemental analysis was conducted to obtain the N-functionalization degree of the various synthesized carbon supports. All synthesized samples reveal a nominal N loading in the range of 0.73–1.29 wt%, where the excess of the solid N precursors (melamine or cyanamide) was altered accordingly to aim this region (details in experimental section and Table 1). The unmodified carbon KB serves as a reference.

The initial increase in N, H and O content of KBox compared to the pristine KB (Table 3) is caused by the treatment in concerted HNO<sub>3</sub> what is reported in literature to etch the surface creating some carboxylic, hydroxyl and NO<sub>x</sub> groups [45]. After further heat treatment in presence of some solid N-precursors (cyanamide or melamine) the N-content of the pre-oxidized KB increases due to formation of a variety of different N-functional groups as pyrrole, pyridine, quaternary N, pyridine-N-oxide and NO<sub>x</sub> [10,29]. At the same time the C-content increases from 90.0 to 95.39–95.74 wt% simultaneously as the oxygen groups vanish and reduces the O-content from 9.68 down to 2.97–3.88 wt%. This shows the low thermal stability of the initial carboxylic and hydroxyl groups and indicates the conversion of such groups into N-functional groups in presence of a N-source.

In the case where unmodified KB was annealed in the presence of either melamine or cyanamide, the carbon content decreases (from 98.57 wt% to 96.19–97.65 wt%) in exchange for an increase in both nitrogen and oxygen content. Under the operation temperature, cyanamide and melamine tend to decompose/convert into hydrogen cyanide (HCN) [46], which enables a surface modification of the carbon support. The overall O and N-content goes down as a function of temperature in favor of the C-content, indicating the thermal decomposition of some less stable N-groups with increased temperature.

The carbon content obtained here via CHNO analysis (Table 3) agrees very well with that determined using XPS and TGA analysis (see details in SI and Fig. S3).

#### 4.3. X-ray photoelectron spectroscopy

The chemical composition and quantitative determination of the N-containing functional groups on the various carbons support was evaluated by X-ray photoelectron spectroscopy (XPS). Evident from Table 4, the pyridinic and pyrrolic groups comprise the majority of N-functional groups, while graphitic groups display only a minor contribution. A correlation with the treatment temperature for the melamine treated carbons with respect to the fractions of pyridinic and pyrrolic groups is discernable (samples KB-Mel-600 and KB-Mel-800, see Table 4 and Figs. S4, S5). The pyridinic groups fraction increases while the pyrrolic fraction decreases in percentage as a result of higher heat treatment temperature [36]. Interestingly, all pre-oxidized carbons treated at 600 °C (KBox-Mel-600 and KBox-CA-600) reveal a decreased fraction of pyridinic/pyrrolic groups in favor of quaternary/-NO<sub>x</sub> groups if comparing to KB-Mel-600 and KB-CA-600. On the other hand, KBox-Mel-600 is the only sample that exhibits an increased pyrrolic

**Table 4**

Summary of XPS composition of the different types of carbons deconvoluted for five N-functionalities. Their content is given as fraction of one specific group over the entire amount of N, so it sums up at 100% overall different N-groups.

Samples	Relative N group content (%)				
	Pyridinic	Pyrrolic	Quaternary	Graphitic	-NO <sub>x</sub>
KBox	0	0	0	0	100
KB-Mel-600	48.7	25.8	9.7	5.8	10.0
KBox-Mel-600	44.9	27.2	12.1	4.0	11.8
KB-Mel-800	49.2	18.4	13.5	4.3	14.6
KB-CA-600	47.6	30.0	7.1	5.8	9.5
KBox-CA-600	42.9	24.9	14.3	3.7	14.2
KB-CA-800	53.5	16.9	13.0	5.0	11.6

fraction. Furthermore, it seems that the fractions of quaternary groups increase with pre-oxidization and treatment temperature for all samples. The NO<sub>x</sub> groups show the most complex trend and seem to increase with pre-oxidation step and increasing temperature. All above present the striking difference of the samples in chemical nature as a result of different modification and synthetic conditions. Hence, the ratio of various N-species may be tuned by adjusting the synthetic route, heat treatment temperature and the N-source.

#### 4.4. Porosity analysis

N<sub>2</sub> adsorption isotherm analysis was applied to evaluate the carbon microstructure and its changes, which could affect several electrochemical parameter of the catalyst layer [47]. Table S5 summarizes the BET and the QSDFT analysis results (see Supplementary information). By using QSDFT calculation, we were able to differentiate between micro- and mesopore contribution to the total area surface (see experimental for more details). Overall, the area of the micropores (< 2 nm) exhibited small variations among all N modified samples, as well as compared to the unmodified KB. These observed differences could be attributed to micropore blockage by the presence of functional groups [5,48]. For all functionalized carbons, the increase of the heat treatment temperature from 600 °C to 800 °C resulted in a small increase of both the micro and mesoporous structure. The latter is clearly caused by the loss of less stable O-containing functional groups during heat treatment at 800 °C. This is in perfect agreement with the TGA data (Fig. S3), where the KB-CA-800 and KB-Mel-800 showed no loss of surface groups during ramping up to around 700 °C, confirming that the less stable surface groups had already been removed during the heat treatment. This is further verified by the oxygen and N content from the elemental analysis (Table 3). As shown in Fig. 1, the cyanamide modified samples reveal a slight decrease in the overall surface area, which is mainly caused by a reduction in mesopore fraction. On the other hand, no drastic changes are discernable for the overall surface area of the Melamine modified ones. Upon closer look into the micro/meso pore ratio, KBox-Mel-600 exhibits an increased fraction of mesopores compared to micropores after N-modification (Table S5). This increased mesopore fraction might reduce mass transport resistance through the catalyst layer. By contrast, reduced mesopore fraction within cyanamide modified samples might contribute to flooding effect under wet operating conditions during in situ MEA testing.

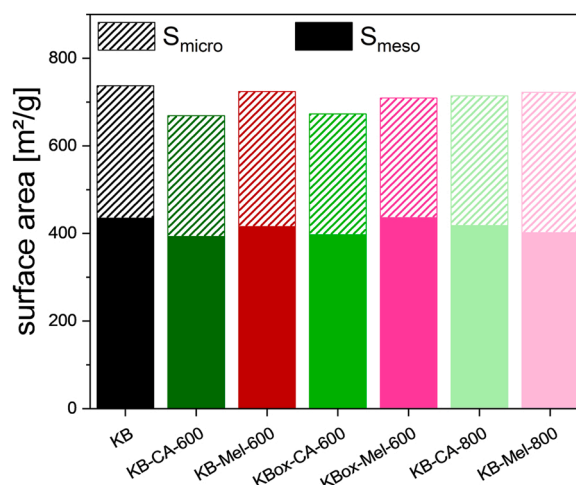


**Fig. 1.** Pore analysis of the carbon structure: microporous surface area ( $S_{\text{micro}}$ ), mesoporous surface area ( $S_{\text{meso}}$ ) and sum of micro- and mesoporous surface area ( $S_{\text{micro}} + S_{\text{meso}}$ ), as calculated using QSDFT, and their corresponding ratio ( $S_{\text{micro}}/S_{\text{meso}}$ ) for each type of carbon used in the present study.

#### 4.5. Hydrophilicity of N doped carbons

Water uptake measurements were conducted to evaluate how physical properties as wettability and water retention change with the N-modification. Fig. 2 depicts the results for 5 selected carbon supports. The hysteresis shape of the water uptake isotherm is similar for all the different carbon materials and indicates a surface behavior of hydrophobic nature. At RH values close to 100%, the equilibration points might slightly vary resulting in small artificial measurement differences at such RH values. So, we can deduce that the overall water uptake is similar for all the samples except KB-Mel-600 which is slightly reduced. This can be attributed to the difference in micro/meso pore structure as discussed above.

To interpret the hydrophilicity behavior of the N-modified samples based on the water uptake measurement, the adsorption branch in the range of 40–80% RH shall be taken in consideration. The easier some water molecules will get adsorbed by the surface, the steeper the increase of the isotherm gets in this region following the more hydrophilic the sample behaves. Thus, the water uptake trends are in the sequence of KBox-CA-600 > KB-CA-800 > KB-CA-600 > KB > KB-Mel-600. All N-modified carbons except KB-Mel-600 exhibited slightly higher hydrophilicity compared to the pristine KB. Nevertheless, no significant differences among the samples were observed in the H<sub>2</sub>O adsorption branch, implying that different N groups have only slightly changed the surface hydrophobicity. Interestingly, in the H<sub>2</sub>O desorption branch, all N-modified carbons exhibited similar hysteresis (30–60% RH) as the reference KB, suggesting similar water retention ability with the unmodified carbon. This is also confirmed by normalization of the isotherms to the BET surface area (Fig. S6), hereby excluding any effects from the overall absolute surface. The observations regarding the water retention ability seem to be N-source specific, as it has been reported that modification of the carbon surface using NH<sub>3</sub> gas increases the water retention ability [49]. Additionally, to rationalize and exclude the impact of later Pt deposition on the hydrophilicity, the water uptake isotherm of pristine KB was compared with the Pt/KB catalyst, depicted in Fig. S7. It is shown that the hydrophilicity does not change with Pt, but the blocking effect of the Pt nanoparticles is indicated by the reduced overall water uptake. Based on all the above, it is clear that the N-modification (using cyanamide or melamine) or presence of Pt did not significantly alter the hydrophilicity, nor did it increase the water retention ability of the carbon support. Therefore, it is expected that these N-modified carbons will not be able to retain additional water between the ionomer and carbon, and hence would not result in any improvement in the proton conductivity at low relative humidities

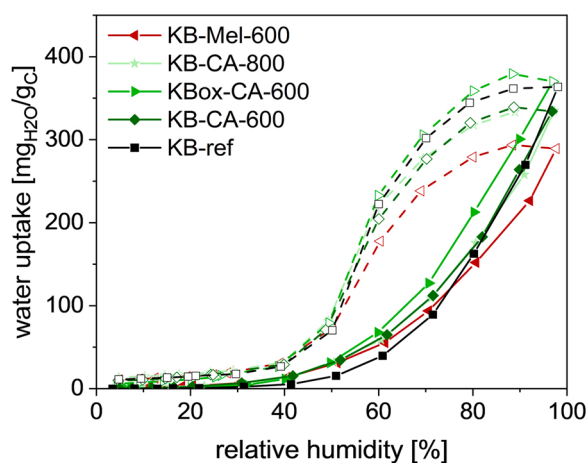


Fig. 2. Water uptake determination of the different carbon supports by water adsorption isotherm ( $\text{mg}_{\text{H}_2\text{O}}/\text{g}_\text{C}$ ) as a function of relative humidity at 298 K. Solid lines illustrate the adsorption curve, whereas dashed lines the desorption curve. KB, KB-CA-600, KBox-CA-600, KB-CA-800, KB-Mel-800.

compared to the unmodified carbons.

#### 4.6. XRD and Pt crystallite/particle size evaluation

To investigate the crystallite size of all the Pt-catalysts supported on N-modified and pristine carbon, XRD measurement was conducted (Fig. S8). As shown in Table 2, all the Pt nanoparticles reveal a similar size in the range of 1.9–2.2 nm. Additional TEM evaluation shows a similar Pt particle size and distribution over all the different catalysts (Fig. S9). The latter, revealed a slightly increased size compared to XRD evaluation ranging from 2.3 to 3.3 nm (refer to Table 2). Hence, all observed differences in MEA performance, which will be thoroughly discussed in the following sections, cannot be rationalized by particle size deviations. The N-modification used in this study does not influence the Pt particle deposition/growth during the polyol-method.

#### 4.7. Effect of N-functionalization on PEMFC performance

In order to better understand the operating range and the effect of different N-modification on the performance, detailed electrochemical characterizations were performed.

To investigate the catalyst layer under two extreme conditions, the in situ operational conditions were set as 60 °C and 90% RH, herein denoted as “wet operating conditions”, and at 90 °C and 30% RH, herein denoted as “dry operating conditions”. The MEA polarization curves under wet and dry operating conditions are given in Figs. S10 and S11, respectively.

Fig. 3 illustrates the performance of the MEAs at two chosen current densities. In the case of “wet operating conditions” (Fig. 3a), it is evident that the MEAs prepared using Pt/KB-Mel-600, Pt/KBox-Mel-600, and Pt/KB-Mel-800 catalysts exhibited the highest performance. In contrast, Pt/KBox-CA-600 and Pt/KB-CA-800 exhibited poor performance that was even lower than the unmodified Pt/KB. These two types of MEAs exhibited signs of electrode flooding even at low current densities (refer to Fig. S10), which can partially be rationalized by the changes in mesoporous structure, as described in section “Porosity analysis”. Water removal properties of the CL are especially critical for high current density performances of MEA, as a significant amount of liquid water is generated and will lead to severe additional O<sub>2</sub> transport resistance if not removed efficiently. The voltage drop in Fig. S10 at high current density in the mass transport region might also be caused to a certain degree by an inhomogeneous ionomer distribution. This in turn would drastically hinder gas transport through the catalyst layer, especially if combined with an ionomer swelling under such wet operating conditions (60 °C and 90% RH) [31]. Such flooding effect under wet operating conditions are known to be correlated with CL micro/mesoporosity [47]. In order to prove our hypothesis, the effect of the ionomer distribution on the blockage of the porous structure of the electrode layer was investigated via N<sub>2</sub> adsorption isotherms [31,50]. An increased fraction of microporosity is discernable for the sample KBox-CA-600/ionomer compared to the unmodified carbon (Fig. S12b), which would explain its particular poor performances in the wet polarization curve, supporting our hypothesis for local electrode flooding as a result of uneven ionomer distribution within the CL. However, since all the N modified carbons exhibited almost identical fractions of micro porosity (Fig. S12b) and therefore similar ionomer fractions among them, it is therefore clear that the homogeneity of the proton conductive pathway is not the only parameter that affects the fuel cell performance.

Fig. 3b depicts the performances under “dry operating conditions”, herein the effect of the ionomer distribution would be better observable since ill-distributed ionomer would reveal a poor proton conducting pathways thus result in low performing MEAs, especially at relatively high current densities [31]. Furthermore, an unevenly distributed ionomer layer would cause ionomer agglomerates, resulting in an additional hindrance for oxygen transport through the catalytic layer [8]. Additionally, the catalyst layer itself including the pore structure of the

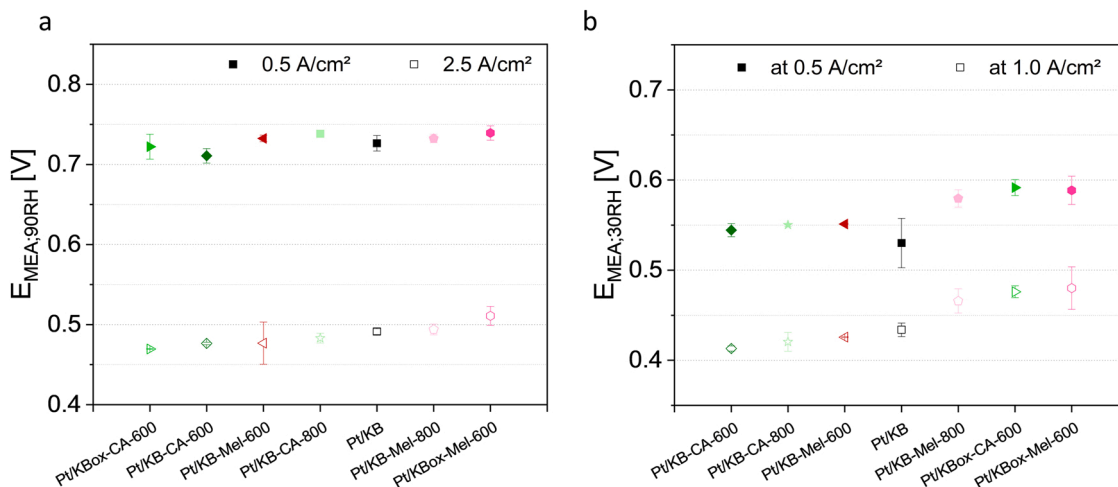


**Fig. 3.** Effect of the cathode catalyst type on the 5 cm<sup>2</sup> MEA performance under various operating conditions. a) At 60 °C, 90% RH and b) at 90 °C and 30% RH. In both cases, a backpressure of 170 kPa<sub>abs</sub> were applied for both anode and cathode compartments. The measurements were conducted under constant differential flow (H<sub>2</sub>: 1.0 NL/min and air: 2.0 NL/min). The voltage was corrected for the monopolar plate resistance (0.0345 Ω cm<sup>2</sup>). The hollow symbol corresponds to the voltage in the low current density region (at 0.5 A/cm<sup>2</sup>), the filled symbol to a high current density (at 2.5 A/cm<sup>2</sup> at 90% RH and 1.0 A/cm<sup>2</sup> at 30% RH). Error bars represent the mean absolute deviation from two independent measurements. The catalysts are sorted based on their performance at the high current density in both subfigures.

support can have a crucial impact on reactant transport. It is evident that the CLs comprising Pt/KBox-Mel-600 exhibits the least voltage losses among all the samples, which would suggest an enhanced reactant transport pathway. Contrary, Pt/KB-CA-600 exhibited the lowest performance compared to all N-modified carbon. These findings correlate with the structural changes in mesopore region (refer to Fig. 1) and the impact of these changes on the mass transport pathways through the catalyst layer. Even though the chosen solid N-precursors does not seem to improve ionomer distribution (as shown in Fig. S12b), the presence of the N-groups or the carbon modification process clearly affects the overall MEA performance. In order to better understand the above-mentioned correlation among the Pt availability in the CL with respect to RH, ionomer coverage and other electrochemical characteristics will be examined in the following section.

#### 4.8. Correlation of Pt availability and ionomer coverage with other electrochemical characteristics

In order to gain a deeper insight in the origin of the observed

performance differences, extensive electrochemical characterization was conducted under different RHs, including CO stripping for the ECSA determination, EIS in H<sub>2</sub>/N<sub>2</sub> for CL proton conductivity (see SI for details, Figs. S13–S15) and limiting current measurements for the mass transport evaluation (see SI for details, Fig. S16). Fig. 4 illustrates a spider diagram which correlates the in situ electrochemical characteristics of the MEAs under both wet and dry operating conditions. Overall, the catalyst covering a larger area in the spider diagram possesses the most favorable electrochemical properties, which would contribute to the improved performance under both operating conditions.

Under wet operating conditions (Fig. 4, blue values), only a weak correlation can be observed between the cell performance and other electrochemical characteristics. All CLs exhibited  $R_{PI}$  (pressure independent term of the total O<sub>2</sub> mass transport resistance) in a comparable range of 0.20–0.24 s/cm at 100% RH. Therefore, the performance differences observed at high current densities (Fig. 3a) have most likely originated from local flooding within the CLs during the acquisition of the polarization curves, where high water production rates are present (note that flooding does not occur during the limiting current

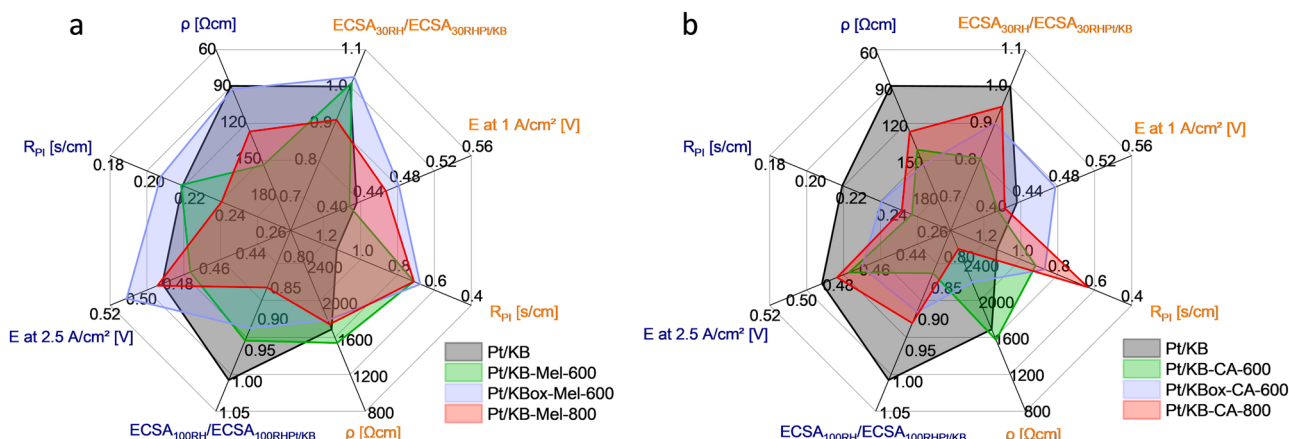


**Fig. 4.** Spider diagram depicting the correlations of all electrochemical characterizations: ECSA, pressure independent mass transport resistance ( $R_{PI}$ ), proton resistivity ( $p$ ) and cell voltage ( $E$ ) at high current density. Orange values represent the data obtained at 30% RH, while the blue colored values at 100% RH. All parameters are given as absolute values except ECSA. For comparison reasons, the ECSA values are normalized to the corresponding value of Pt/KB at 30% and 100% RH, respectively. The exact data with the corresponding error bars can be found in Figs. 3, S13, S16 and Table S3. Whereas the error bars represent the mean absolute deviation from two independent measurements.



measurement due to significantly less water production under diluted O<sub>2</sub> condition). In addition, the proton resistivity ( $\rho$ ) gives a macroscopic value for the protonic pathway throughout the entire catalyst layer. By comparing Pt/KB with Pt/KB-Mel-800 and taking the slight differences of  $\rho$ -values across all the tested CLs into consideration, it is clear that the observed performance difference depicted in Fig. 4a under wet conditions cannot be rationalized based on proton transport resistivity. The accessibility of the Pt sites in the catalyst layer for each sample can be estimated using the Pt utilization efficiency, given in Table S2. The Pt efficiency is calculated by dividing the ECSA under wet operating conditions (100% RH) obtained via CO stripping in MEA with the theoretical ECSA derived from the average Pt particle size measured by TEM. Under wet conditions (100% RH), it is expected that the majority of the Pt particles present in the micropores are being electrochemically active [47,51]. The Pt utilization efficiency of Pt/KB-Mel-800 and Pt/KB-CA-600 correlates with the MEA performance under wet operating conditions, revealing an increase and decrease in performance, respectively. Contrary, Pt/KBox-CA-600 shows decreased performance even though providing the highest Pt utilization efficiency. This might lie in a more pronounced flooding effect counteracting the beneficial utilization effect.

By lowering the relative humidity to 30%, the effects of altered ionomer distributions and the porous structure on the mass transport resistance become more pronounced. However, as shown in Fig. 4, for all the catalyst samples, the MEA performance under dry conditions cannot be directly correlated with the proton resistivity values. Fig. 4 clearly evidences that the N-modified carbons exhibited similar and, in some cases, even higher proton resistivity in the CL compared to the reference KB. This confirms that the N-functionalization of the carbon support, applying either melamine or cyanamide, did not result in an enhancement of proton transport by a more uniform ionomer distribution. These findings are also in perfect agreement with the findings depicted in Fig. S12b. In addition, KB-CA-800 and KBox-CA-600 exhibited the highest CL proton resistivity among all supports, yet the fuel cell performance (illustrated in Fig. 3) of the KBox-CA-600 was amongst the highest. This suggests that the proton conductive pathway alone does not solely explain the differences in the observed performances.

As evident in Fig. 4, there exists no clear correlation between the performance and the ECSA under dry operating conditions. Furthermore, Fig. 4 reveals that Pt/KBox-Mel-600, Pt/KB-Mel-800 and Pt/KB-CA-800 exhibit the lowest total mass transport resistances under dry operating conditions among all tested catalysts, while these are among the highest performing catalysts, as well (Fig. 3 and Fig. S16). This is not the case for Pt/KB-CA-800, the performance of which drops significantly despite having reasonably good oxygen transport pathways. This can be rationalized by the increased proton transport resistance originated from an unfavored proton conducting pathway throughout the catalyst layer. By comparing the trends in Fig. 4, it can be shown that the mass transport resistance of the Pt/ionomer interface (included in the pressure independent term of the mass transport resistance) is not inverse proportional to the ECSA for some of the catalysts (e.g. KB-CA-600 and KB-Mel-800). According to the fundamental derivation and calculation of  $R_{PI}$  there is a direct correlation with the inverse ECSA. Thus a reduced ECSA should increase mass transport resistance [52]. Nevertheless N-modified supports deviate from this trend. KB-CA-600 and KBox-CA-600 (Fig. S16), for instance, exhibit the highest mass transport resistance values among all supports under dry conditions (30% RH). While they share similar  $R_{PI}$  and total mass transport resistance, KB-CA-600 has significantly less ECSA at 30% RH between both. A plausible explanation of this effect lies in the structure of the Pt/ionomer interface (Coulombic interaction), where dry operating condition could affect the adsorption of ionomer sulfonic acid groups on the Pt active sites and possibly alter the electronic status, which would in turn result in an increase of mass transport resistance at the Pt/ionomer interface [43,44]. It is well known that  $R_{PI}$  mainly comprises the oxygen transport

resistances arising from Knudsen diffusion [8] as well as the diffusion resistance through the ionomer towards the catalyst active sites. Therefore, the difference in  $R_{PI}$  observed at 30% RH could also be attributed to the difference in carbon micro/mesoporous structure, and the ionomer distribution/blockage of the porous structure. This demonstrates the interplay and correlation of the physicochemical carbon properties with the in-situ fuel cell operation. From the correlation under dry operating conditions, it becomes clear that the mass transport resistance is the most influential factor on the MEA performance in the present case. Despite this, one can clearly see the complexity and the interplay of the different physicochemical and electrochemical parameters determining the overall CL performance. Therefore, factors such as porosity and wettability will determine the resulting ionomer and pore size distribution in the catalyst layer. Following in-situ characteristics like mass transport and proton resistivity, both are linked to the ex-situ evaluated material properties. To develop an optimized catalyst layer the interplay and fine-tuning of all those different abovementioned parameters need to be considered/optimized.

#### 4.9. Molecular catalyst support/ionomer interactions

To gain a deeper understanding of the interaction between the carbon support and the ionomer, XPS evaluation and analysis were conducted. For this purpose, a set of pure N-modified carbon samples were compared to the same set of carbon species coated with ionomer. In order to ensure a sufficient surface sensitivity of XPS, the I/C ratio in this case was not higher than 0.25, significantly lower than that used for MEA manufacturing.

As mentioned in the experimental section, 5 peak components were applied to fit the pure N-carbon species: pyridinic-N, pyrrolic-N, quaternary-N, graphitic-N and NO<sub>x</sub>. Hereby the pyrrolic-N groups comprise of pyrrole, imides, amine, amide and lactam, which reveal similar eV shifts (Fig. 5a). In the presence of ionomer covering the different carbon supports, the aforementioned set of N-functional groups is no longer sufficient to differentiate the different N-groups of the sample and to fit the spectra accurately. Therefore, it has to be extended by three additional groups referring to protonated N-species [35–39, 53–56]. An exact table is given in Supplementary information (Table S4).

In our previous study using NH<sub>3</sub> for carbon modification [49], we already reported a shift in the binding energy to higher values in XPS N1s spectra due to ionomer↔N-group interaction. A similar shift in the binding energy is also observed here (Fig. 5a) after coating ionomer on the N-carbon modified carbon supports using solid precursors. The strong acidic character of the ionomer result in a protonation of the N-groups caused by a Brønsted acid-base interaction between the acidic sulfonate sidechain and the basic N-species. The N-groups reveal a depletion in local electronic density near the N-core consequently shifting the entire spectrum towards higher binding energy. In our recent work [49], we clearly observed a correlation between the fraction of the charged species and the MEA performance, caused by a more homogeneous ionomer distribution after N-modification of the carbon support with NH<sub>3</sub> gas. This seems to be quite specific for NH<sub>3</sub>-modified samples. In the present case where melamine and cyanamide were used to modify the carbon surface, the physicochemical properties of the N-carbon and the resulting Pt-catalyst appear quite differently. The N-modification and interaction with the ionomer does not show improvement in ionomer distribution but rather influence the porous character of the support as mentioned above. Evident from Fig. 5b, in the current case using N solid precursors, the number of protonated species (including protonated pyridinic-N and remaining hydrogenated-N groups as lactam, imine, etc. herein denoted as hydrogenated groups) does not seem to correlate significantly with the overall MEA performance. A possible explanation of this might be a threshold value of the pyridinic groups content. As we pointed out in our recent work, pyridinic Ns are favorably protonated by the ionomer



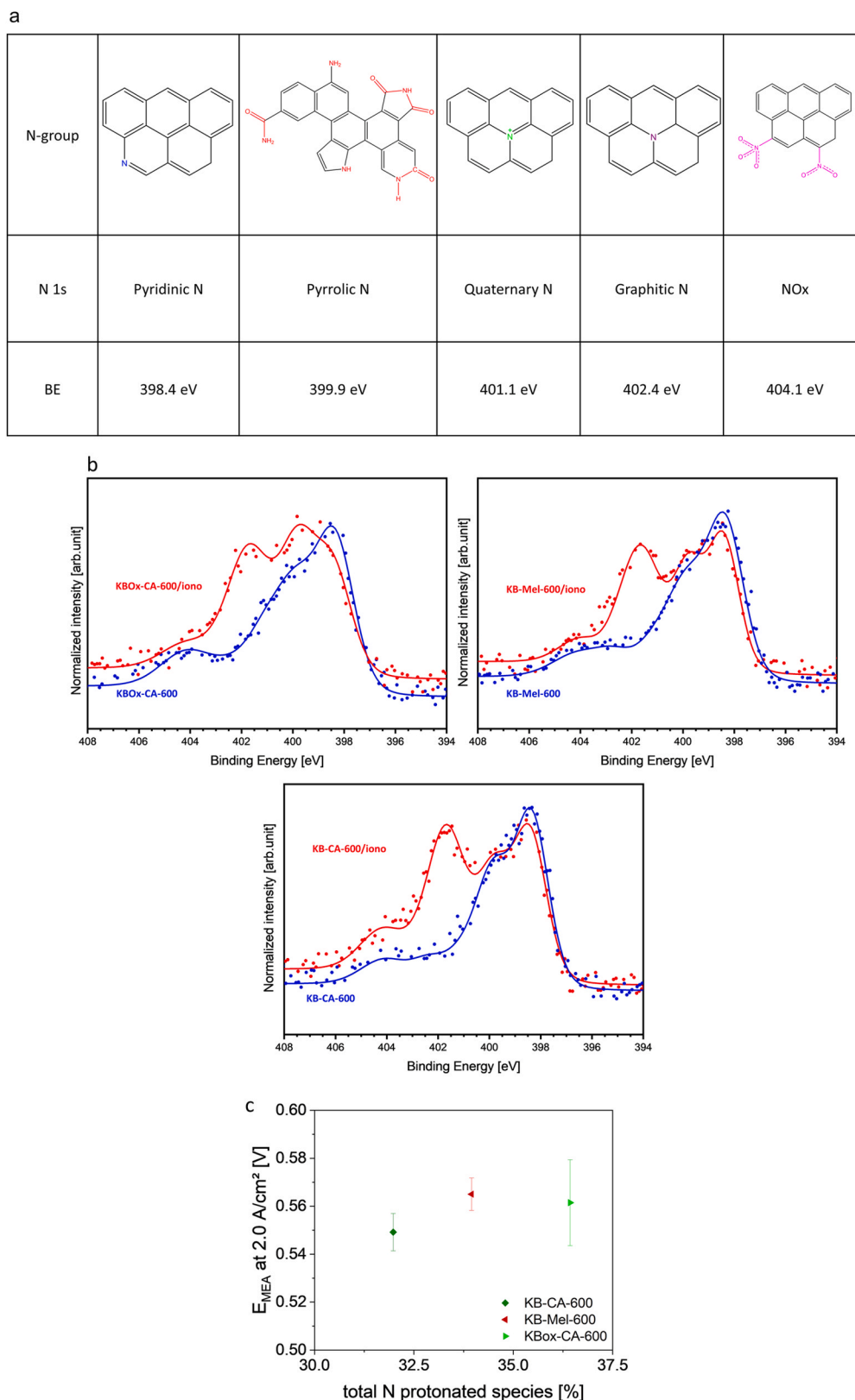


**Fig. 5.** a) Table of schematic scheme of different types of N functionalities in the C matrix and their corresponding binding energy (BE) deconvoluted from N 1s photoemission spectra [36,53,54,57]. The N-functionalities are grouped as pyridinic, pyrrolic, quaternary, graphitic and NOx ones whereas the pyrrolic group also includes imides, amine, amide and lactam which reveal similar eV shifts. b) XPS spectra of the N1s region in the N-modified KB (KB-CA-600, KBOx-CA-600 and KB-Mel-600) compared with the corresponding ionomer coated carbon support. c) Correlation of the total N protonated species (sum of “protonated” and “hydrogenated” N-groups) in the C/ionomer coating with the performance of the corresponding Pt/C electrode at high current density at 90% RH and 60 °C at 2 A/cm<sup>2</sup>. The error bars represent the mean absolute deviation from two independent measurements.

generating a positively charged N-specie [49]. This protonation process accumulates positive charge on the carbon surface thus there might be a limit in such surface charge preventing further protonation of the remaining pyridinic N-groups. Consequently, carbon containing a N-pyridine content above such threshold value will also reveal an increased content of unprotonated/uncharged pyridine groups in the resulting electrode layer after ionomer coating. Those remaining groups might be unfavorable for a homogenous ionomer distribution and counteract the beneficial effect of protonated pyridinic groups. Additionally, in contrast to melamine or cyanamide modified carbons, water uptake measurements show an increase in hydrophilicity for ammonia modified ones. The latter might improve the wettability of the carbon support during ink manufacturing and promote an even distribution of the ionomer. Nevertheless, we prove an interaction between the N-groups and the ionomer what is crucial for further catalyst layer development, since we point out the importance of the type of precursor, the N-groups itself and the synthetic route for the tailoring of new support materials.

## 5. Conclusion

The present study investigates the effect of chemical surface modifications of carbon support materials using N solid precursors on the power performance of low Pt-loaded MEA cathodes. The surface and bulk composition of the various N-doped carbon supports were investigated using XPS and Elemental analysis. Analysis of the resulting surface area and micropore structure of the N-doped carbon supports, a clear influence of the thermal heat treatment and of the type of solid precursor on the resulting surface properties emerged. Additional water adsorption isotherms evaluation revealed that the presence of N groups on the carbon supports neither significantly affected the hydrophilicity of the supports, nor presented enhanced water retain ability compared to the unmodified carbon support.

In order to shed more light onto the origin of the performance difference between samples, the MEAs were subjected to extreme operating conditions as either wet (at 60 °C, 90% RH) or dry (at 90 °C, 30% RH) ones, where the voltage losses within the CL change drastically with synthetic route of N-modification. The combination of these two working conditions combined with limiting current and EIS measurements, helped us to explain the outstanding performance of some N-modified catalysts as Pt/KB-Mel-800 and Pt/KBox-Mel-600 verses others. Their improved performance results from an increase in oxygen mass transport, which is hypothesized to originate, in turn, from the alteration of carbon porous structure during the synthetic process. Intriguingly, the use of N solid precursors for N modification of the carbon support surface seem to have resulted in neither an improvement of the proton conductive pathway, nor the ECSA of the cathodic catalyst layer, when compared to an unmodified carbon support. This suggests, in contrast to earlier conventional wisdom, that N-modification itself does not always lead to a more evenly distributed ionomer layer in the CL. Rather, improved homogeneity does depend on other physicochemical and surface properties of the carbon supports, as well, underlining the complexity of the phenomenon.

## CRedit authorship contribution statement

A.O. conceived the project. S.O. synthesized all the samples and carried out catalyst characterization as N<sub>2</sub> physisorption, ICP, TGA and XRD. F.D. and A.O. carried out the MEA manufacturing, fuel cell experiments and data analysis. L.L. and B.C. conducted and analyzed XPS measurements. S.S. carried out TEM measurements. T.A.D. evaluated proton resistivity measurements. P.S. provided guidance and constructive ideas throughout the project to ensure the successful outcome of this project. All authors contributed to the discussion part, drew conclusions and participated in finalizing the text and figures.

## Declaration of Competing Interest

The authors declare that they have no known competing financial interests or personal relationships that could have appeared to influence the work reported in this paper.

## Acknowledgement

This work was supported by the BMW Group. The authors would also like to thank the members of FC Test Field, FC Technology Development and Technology Material Analysis of BMW Group for their support during Fuel cell testing, MEA manufacturing and decal preparation. Special thanks goes to Steffen Hausdorf from TU Dresden for conducting water uptake measurements and the following fruitful discussions interpreting the results.

Furthermore, M.L.L. acknowledges the financial support from the National Council of Science and Technology of Mexico (CONACyT, Grant 708585) and the support by the Deutsche Forschungsgemeinschaft (DFG, German Research Foundation) under Germany's Excellence Strategy – EXC 2008 – 390540038 – UniSysCat.

## Appendix A. Supporting information

Supplementary data associated with this article can be found in the online version at doi:10.1016/j.apcatb.2022.121118.

## References

- [1] O. Gröger, H.-A. Gasteiger, J.-P. Suchsland, Review—electromobility: batteries or fuel cells? *ECS* 162 (2015) A2605–A2622.
- [2] A. Kongkanand, M.F. Mathias, The priority and challenge of high-power performance of low-platinum proton-exchange membrane fuel cells, *J. Phys. Chem. Lett.* 7 (2016) 1127–1137.
- [3] Y.-C. Park, H. Tokiwa, K. Kakinuma, M. Watanabe, M. Uchida, Effects of carbon supports on Pt distribution, ionomer coverage and cathode performance for polymer electrolyte fuel cells, *J. Power Sources* 315 (2016) 179–191.
- [4] ([https://energy.gov/sites/prod/files/2014/02/f8/fctt\\_roadmap\\_june2013.pdf](https://energy.gov/sites/prod/files/2014/02/f8/fctt_roadmap_june2013.pdf)), (08/21/18).
- [5] A. Orfanidi, P. Madkikar, H.A. El-Sayed, G.S. Harzer, T. Kratky, H.A. Gasteiger, The key to high performance low Pt loaded electrodes, *J. Electrochem. Soc.* 164 (2017) F418–F426.
- [6] A. Ohma, T. Mashio, K. Sato, H. Iden, Y. Ono, K. Sakai, K. Akizuki, S. Takaichi, K. Shinohara, Analysis of proton exchange membrane fuel cell catalyst layers for reduction of platinum loading at Nissan, *Electrochim. Acta* 56 (2011) 10832–10841.
- [7] V. Yarlagaadda, M.K. Carpenter, T.E. Moylan, R.S. Kukreja, R. Koestner, W. Gu, L. Thompson, A. Kongkanand, Boosting fuel cell performance with accessible carbon mesopores, *ACS Energy Lett.* 3 (2018) 618–621.
- [8] S. Ott, A. Orfanidi, H. Schmies, B. Anke, H.N. Nong, J. Hübner, U. Gernert, M. Glieth, M. Lerch, P. Strasser, Ionomer distribution control in porous carbon-supported catalyst layers for high-power and low Pt-loaded proton exchange membrane fuel cells, *Nat. Mater.* 19 (2020) 77–85.
- [9] H. Yang, Y. Ko, W. Lee, A. Züttel, W. Kim, Nitrogen-doped carbon black supported Pt–M (M = Pd, Fe, Ni) alloy catalysts for oxygen reduction reaction in proton exchange membrane fuel cell, *Mater. Today Energy* 13 (2019) 374–381.
- [10] B. Zhang, Z. Wen, S. Ci, S. Mao, J. Chen, Z. He, Synthesizing nitrogen-doped activated carbon and probing its active sites for oxygen reduction reaction in microbial fuel cells, *ACS Appl. Mater. Interfaces* 6 (2014) 7464–7470.
- [11] N.P. Subramanian, X. Li, V. Nallathambi, S.P. Kumaraguru, H. Colon-Mercado, G. Wu, J.W. Lee, B.N. Popov, Nitrogen-modified carbon-based catalysts for oxygen reduction reaction in polymer electrolyte membrane fuel cells, *J. Power Sources* 188 (2009) 38–44.
- [12] Y. Liu, X.-J. Jin, D.D. Dionysiou, H. Liu, Y.-M. Huang, Homogeneous deposition-assisted synthesis of iron–nitrogen composites on graphene as highly efficient non-precious metal electrocatalysts for microbial fuel cell power generation, *J. Power Sources* 278 (2015) 773–781.
- [13] W.H. Lee, D.W. Lee, H. Kim, Development of nitrogen-doped carbon catalysts using melamine-based polymer as a nitrogen precursor for the oxygen reduction reaction, *ECS* 162 (2015) F744–F749.
- [14] H.T. Chung, C.M. Johnston, K. Artyushkova, M. Ferrandon, D.J. Myers, P. Zelenay, Cyanamide-derived non-precious metal catalyst for oxygen reduction, *Electrochem. Commun.* 12 (2010) 1792–1795.
- [15] P.Q. Phan, R. Narapratwaphong, P. Pornaroontham, J. Park, C. Chokradjaroen, N. Saito, N-Doped few-layer graphene encapsulated Pt-based bimetallic nanoparticles via solution plasma as an efficient oxygen catalyst for the oxygen reduction reaction, *Mater. Adv.* 2 (2021) 322–335.

- [16] G. Massaglia, A. Sacco, M. Castellino, A. Chiodoni, F. Frascella, S. Bianco, C.F. Pirri, M. Quaglio, N-doping modification by plasma treatment in polyacrylonitrile derived carbon-based nanofibers for oxygen reduction reaction, *Int. J. Hydrog. Energy* 46 (2021) 13845–13854.
- [17] X. Yan, F. Zhang, H. Zhang, H. Tang, M. Pan, P. Fang, Improving oxygen reduction performance by using protic poly(ionic liquid) as proton conductors, *ACS Appl. Mater. Interfaces* 11 (2019) 6111–6117.
- [18] J.A. Priithi, N. Rajalakshmi, G. Ranga, Rao, Nitrogen doped mesoporous carbon supported Pt electrocatalyst for oxygen reduction reaction in proton exchange membrane fuel cells, *Int. J. Hydrog. Energy* 43 (2018) 4716–4725.
- [19] E.N. Gribov, A.N. Kuznetsov, V.A. Golovin, D.V. Krasnikov, V.L. Kuznetsov, Effect of modification of multi-walled carbon nanotubes with nitrogen-containing polymers on the electrochemical performance of Pt/CNT catalysts in PEMFC, *Mater. Renew. Sustain. Energy* 8 (2019) 7.
- [20] H. Schmies, E. Hornberger, B. Anke, T. Jurzinsky, H.N. Nong, F. Dionigi, S. Kühl, J. Drnec, M. Lerch, C. Cremers, P. Strasser, Impact of carbon support functionalization on the electrochemical stability of Pt fuel cell catalysts, *Chem. Mater.* 30 (2018) 7287–7295.
- [21] Z. Fang, M.S. Lee, J.Y. Kim, J.H. Kim, T.F. Fuller, The effect of carbon support surface functionalization on PEM fuel cell performance, durability, and ionomer coverage in the catalyst layer, *J. Electrochem. Soc.* 167 (2020), 064506.
- [22] A. Öztürk, A.B. Yurtcan, Raw and pyrolyzed (with and without melamine) graphene nanoplatelets with different surface areas as PEM fuel cell catalyst supports, *Carbon Lett.* 31 (2021) 1191–1214.
- [23] A. Öztürk, A.B. Yurtcan, Preparation and characterization of melamine-led nitrogen-doped carbon blacks at different pyrolysis temperatures, *J. Solid State Chem.* 296 (2021), 121972.
- [24] S. Woo, S. Lee, A.Z. Taming, T.H. Yang, S.H. Park, S.D. Yim, Current understanding of catalyst/ionomer interfacial structure and phenomena affecting the oxygen reduction reaction in cathode catalyst layers of proton exchange membrane fuel cells, *Curr. Opin. Electrochem.* 21 (2020) 289–296.
- [25] I. Jiménez-Morales, A. Reyes-Carmona, M. Dupont, S. Cavaliere, M. Rodlert, F. Mornaghini, M.J. Larsen, M. Odgaard, J. Zajac, D.J. Jones, J. Rozière, Correlation between the surface characteristics of carbon supports and their electrochemical stability and performance in fuel cell cathodes, *Carbon Energy* 3 (2021) 654–665.
- [26] K. Artyushkova, M.J. Workman, I. Matanovic, M.J. Dzara, C. Ngo, S. Pylypenko, A. Serov, P. Atanassov, Role of surface chemistry on catalyst/ionomer interactions for transition metal–nitrogen–carbon electrocatalysts, *ACS Appl. Energy Mater.* 1 (2017) 68–77.
- [27] L. Pan, S. Ott, F. Dionigi, P. Strasser, Current challenges related to the deployment of shape-controlled Pt alloy oxygen reduction reaction nanocatalysts into low Pt-loaded cathode layers of proton exchange membrane fuel cells, *Curr. Opin. Electrochem.* 18 (2019) 61–71.
- [28] Nathaniel D. Leonard, et al., Deconvolution of utilization, site density, and turnover frequency of Fe–nitrogen–carbon oxygen reduction reaction catalysts prepared with secondary N-precursors, *ASC Catal.* 8 (2018) 1640–1647.
- [29] R.P. Rocha, O.S.G.P. Soares, A.G. Gonçalves, J. Órfão, M. Pereira, J.L. Figueiredo, Different methodologies for synthesis of nitrogen doped carbon nanotubes and their use in catalytic wet air oxidation, *Appl. Catal. A: Gen.* 548 (2017) 62–70.
- [30] Y. Chen, J. Wang, H. Liu, R. Li, X. Sun, S. Ye, S. Knights, Enhanced stability of Pt electrocatalysts by nitrogen doping in CNTs for PEM fuel cells, *Electrochem. Commun.* 11 (2009) 2071–2076.
- [31] A. Orfanidi, P.J. Rheinlander, N. Schulte, H.A. Gasteiger, Ink solvent dependence of the ionomer distribution in the catalyst layer of a PEMFC, *J. Electrochem. Soc.* 165 (2018) F1254–F1263.
- [32] G.Y. Gor, M. Thommes, K.A. Cychoz, A.V. Neimark, Quenched solid density functional theory method for characterization of mesoporous carbons by nitrogen adsorption, *Carbon* 50 (2012) 1583–1590.
- [33] A.V. Neimark, Y. Lin, P.I. Ravikovitch, M. Thommes, Quenched solid density functional theory and pore size analysis of micro-mesoporous carbons, *Carbon* 47 (2009) 1617–1628.
- [34] J. Yeh, I. L. Atomic subshell photoionization cross sections and asymmetry parameters, *At. Data Nucl. Data Tables* 32 (1985) 1–155.
- [35] K. Artyushkova, Misconceptions in interpretation of nitrogen chemistry from x-ray photoelectron spectra, *J. Vac. Sci. Technol. A* 38 (2020), 031002.
- [36] K.F. Ortega, R. Arrigo, B. Frank, R. Schlögl, A. Trunschke, Acid–base properties of n-doped carbon nanotubes: a combined temperature-programmed desorption, X-ray photoelectron spectroscopy, and 2-propanol reaction investigation, *Chem. Mater.* 28 (2016) 6826–6839.
- [37] F. Späth, W. Zhao, C. Gleichweit, K. Gotterbarm, U. Bauer, O. Höfert, H. P. Steinrück, C. Papp, Hydrogenation and dehydrogenation of nitrogen-doped graphene investigated by X-ray photoelectron spectroscopy, *Surf. Sci.* 634 (2015) 89–94.
- [38] R. Arrigo, M. Hävecker, R. Schlögl, D. S.S., Dynamic surface rearrangement and thermal stability of nitrogen functional groups on carbon nanotubes, *Chem. Commun.* (2008) 4891–4893.
- [39] I. Matanovic, K. Artyushkova, M.B. Strand, M.J. Dzara, S. Pylypenko, P. Atanassov, Core level shifts of hydrogenated pyridinic and pyrrolic nitrogen in the nitrogen-containing graphene-based electrocatalysts: in-plane vs edge defects, *J. Phys. Chem. C* 120 (2016) 29225–29232.
- [40] K. Shinozaki, Y. Morimoto, B.S. Pivovar, S.S. Kocha, Suppression of oxygen reduction reaction activity on Pt-based electrocatalysts from ionomer incorporation, *J. Power Sources* 325 (2016) 745–751.
- [41] D.R.C. Baker, C.A. Neyerlin K.C., M.W. Murph, Measurement of oxygen transport resistance in PEM fuel cells by limiting current methods, *J. Electrochem. Soc.* 156 (2009) B991–B1003.
- [42] G. Tsotridis, A. Pilenga, G.D. Marco, T. Malkow, EU harmonised test protocols for PEMFC MEA testing in single cell configuration for automotive applications, *JRC Sci. Hub.* (2015).
- [43] F. Du, T.A. Dao, P. Peitl, A. Bauer, K. Preuss, A.M. Bonastre, J. Sharman, G. Spikes, M. Perchthaler, T.J. Schmidt, A. Orfanidi, Effects of PEMFC operational history under dry/wet conditions on additional voltage losses due to ionomer migration, *J. Electrochem. Soc.* 167 (2020), 144513.
- [44] S.K. Jomori, K. Nonoyama N., M. Kato, T. Yoshida, An experimental study of the effects of operational history on activity changes in a PEMFC, *J. Electrochem. Soc.* 160 (2013) (F1073–F1073).
- [45] X. Li, H. Wang, J.T. Robinson, H. Sanchez, G. Diankov, H. Dai, Simultaneous nitrogen doping and reduction of graphene oxide, *JACS* 131 (2009) 15939–15944.
- [46] X. Liu, J. Hao, S. Gaan, Recent studies on the decomposition and strategies of smoke and toxicity suppression for polyurethane based materials, *RSC Adv.* 6 (2016) 74742–74756.
- [47] N. Ramaswamy, W. Gu, J.M. Ziegelbauer, S. Kumaraguru, Carbon support microstructure impact on high current density transport resistances in PEMFC cathode, *ECS* 167 (2020), 064515.
- [48] M. Toupin, D. Belanger, Spontaneous functionalization of carbon black by reaction with 4-nitrophenyldiazonium cations, *Langmuir* 24 (2008) 1910–1917.
- [49] S. Ott, et al., Understanding the performance increase of catalysts supported on N-functionalized carbon in PEMFC catalyst layers, *JES* (2022) (In preparation).
- [50] Y.-C. Park, K. Kakinuma, H. Uchida, M. Watanabe, M. Uchida, Effects of short-side-chain perfluorosulfonic acid ionomers as binders on the performance of low Pt loading fuel cell cathodes, *J. Power Sources* 275 (2015) 384–391.
- [51] E. Padgett, N. Andrejevic, Z. Liu, A. Kongkanand, W. Gu, K. Moriyama, Y. Jiang, S. Kumaraguru, T.E. Moylan, R. Kukreja, D.A. Muller, Connecting fuel cell catalyst nanostructure and accessibility using quantitative cryo-STEM tomography, *ECS* 165 (2018) F173–F180.
- [52] J.P. Owejan, J.E. Owejan, W. Gu, Impact of platinum loading and catalyst layer structure on PEMFC performance, *J. Electrochem. Soc.* 160 (2013) F824–F833.
- [53] S. Chae, G. Panomsuwan, M.A. Bratescu, K. Teshima, N. Saito, p-Type doping of graphene with cationic nitrogen, *ACS Appl. Nano Mater.* 2 (2019) 1350–1355.
- [54] S. Rojas-Carbonell, K. Artyushkova, A. Serov, C. Santoro, I. Matanovic, P. Atanassov, Effect of pH on the activity of platinum group metal-free catalysts in oxygen reduction reaction, *ACS Catal.* 8 (2018) 3041–3053.
- [55] R.K. Blundell, P. Licence, Quaternary ammonium and phosphonium based ionic liquids: a comparison of common anions, *Phys. Chem. Chem. Phys.* 16 (2014) 15278–15288.
- [56] A.R. Santos, R.K. Blundell, P. Licence, XPS of guanidinium ionic liquids: a comparison of charge distribution in nitrogenous cations, *Phys. Chem. Chem. Phys.* 17 (2015) 11839–11847.
- [57] R. Arrigo, M. Hävecker, R. Schlögl, D.S. Su, Dynamic surface rearrangement and thermal stability of nitrogen functional groups on carbon nanotubes, *Chem. Commun.* (2008) 4891–4893.